Journal of The Electrochemical Society, **158** (12) A1335-A1339 (2011)
0013-4651/2011/158(12)/A1335/5/$28.00 © The Electrochemical Society

In Situ Transmission X-ray Microscopy Study on Working SnO Anode Particle of Li-Ion Batteries

Sung-Chieh Chao,[a] Yu-Chan Yen,[a] Yen-Fang Song,[b,z] Hwo-Shuenn Sheu,[b] Hung-Chun Wu,[c] and Nae-Lih Wu[a,*,z]

[a]*Department of Chemical Engineering, National Taiwan University, Taipei 106, Taiwan*
[b]*National Synchrotron Radiation Research Center, Hsinchu 30077, Taiwan*
[c]*Materials Research Laboratories, Industrial Technology Research Institute, Chutung, Hsinchu 310, Taiwan*

The evolution of the interior microstructures of SnO during electrochemical lithiation/de-lithiation has been visualized by in situ transmission X-ray microscopy (TXM), complemented by in situ X-ray diffraction (XRD) to reveal phase information. A SnO secondary particle consisting of plates of primary particles has been shown to homogeneously expand during the first lithiation in two stages, including the first producing Li_2O matrix that bears most original particle morphology and the second involving full lithiation of the precipitated Sn nano-particles from the first stage. Only the second stage is reversible upon de-lithiation, and the particle undergoes the reversible second-stage deformation during subsequent cycles. The results indicate clear advantages of using such a porous secondary SnO as the anode material in comparison with dense Sn particle previously revealed, including fast lithiation/de-lithiation kinetics, reduced overall volume expansion and enhanced mechanical robustness of the particle, supported by the Li_2O backbones.
 [DOI: 10.1149/2.043112jes]

Manuscript submitted April 15, 2011; revised manuscript received August 8, 2011. Published October 31, 2011.

Lithium-ion batteries are widely regarded as the choice power source for future electric vehicle application. To meet this demand, the specific capacities of both cathode and anode have to be significantly increased from the state-of-the-art values. The currently predominant anode material is graphite, which has a theoretical specific capacity of ca. 370 mAh/g. Several elements, such as Sn,[1,2] which form alloys with Li are potential anode materials with far greater theoretical lithiation capacities. However, these Li-alloying materials all suffer from extensive microstructural deformations, namely expansion and contraction, during electrochemical lithiation and de-lithiation, and these cyclic dimensional variations tend to cause structural instability of the electrode, leading to fast capacity fading. Information regarding the dynamics of these deformation processes would be valuable to the research for establishing viable high-energy anodes based on these materials.

We have recently demonstrated the success of using synchrotron transmission X-ray microscopy (TXM)[3] to reveal the interior microstructure of dense Sn particles during electrochemical lithiation/de-lithiation (L/D) cycles. In such an analysis, Sn particles are dispersed within a free-standing graphite film as the working electrode, which is subsequently assembled with a Li counter electrode to form a "half-cell". High-energy X-ray is allowed to pass through the entire cell as well as individual Sn particles so as to give transmission images of their interior microstructures with a resolution of a few tenths micron.

In this work, we have combined in situ TXM with in situ synchrotron X-ray diffraction (XRD) to study the evolution of the interior microstructures, along with phase composition information, of SnO during electrochemical L/D. SnO exhibits slightly different electrochemical behaviors from Sn. An in-depth review on the electrochemical aspects of Sn-based anodes can be found in Ref. 4. In brief, SnO is known to undergo reduction to form metallic Sn along with inert Li_2O[4–6] upon first lithiation:

$$SnO + 2Li^+ + 2e^- \rightarrow Sn + Li_2O; \qquad [1]$$

and only the resulting Sn is capable of carrying out reversible L/D in the subsequent cycles. Sn can form a series of alloy compounds with Li. Tin oxides have been shown to possess superior cycle stability to pure Sn.[5–8] The results obtained in this work may provide valuable information to the understanding of L/D cycling behaviors of these materials and clues to robust design of Li-alloying anode against capacity fading.

Experimental

Samples and electrode preparations.— SnO powder was used as received (Aldrich) without any treatment. Experiments were carried out by using the 2032-type coin-cells. Fig. 1a shows the assembly of the coin-cells that were used for the synchrotron studies. The working electrode consisted of the SnO particles, conductive additives and binder with weight ratios of 10: 82: 8. The conductive additives include graphitic flakes (KS6, 3 μm, Timcal) and nano-size carbon black (Super P, 40 nm, Timcal) with a weight ratio of 5:1. The binder was a mixture of styrene-butadiene-rubber (SBR; L1571, Asahi Chemicals) and sodium-carboxyl-methyl- cellulose (SCMC; WS-C, Cellogen, DKS International, Inc.) with 1:1 weight ratio. The working electrode was made by coating the slurry mixture containing the above–mentioned solid ingredients on a polymer film (Mylar) to form a continuous top layer. Once dried, the top layer was removed from the substrate to obtain a free-standing film. The film was then roll-compressed to have a final thickness of ca. 50 μm, and working electrode disks of 13 mm in diameter were punched off from the film. Each electrode contained ca. 5.0 mg of the active and conductive materials. The counter electrode was a Li disk (13-mm diameter, 0.3-mm thick), and the electrolyte was 1 M solution of $LiPF_6$ in ethylene carbonate (EC)/ethyl methyl carbonate (EMC) (Zhangjiagang Guotai Ronghua) (1:2 vol.%) with 2 wt% vinylene carbonate (VC). The covers on both sides of the cell were perforated and sealed with Kapton tapes in order to allow the X-ray beam to pass through the cell.

Electrochemical analysis.— The electrochemical L/D processes conducted during the TXM and XRD analyses are the same. The lithiation process includes first a constant-current (0.05 A/g) step from 1.5 V to 0.001 V, followed by a constant-voltage step (0.001 V) with a cut-off current equal to one-tenth of the current value at the first step. The de-lithiation process is carried out only with a constant-current step from 0.001 V to 1.5 V.

Synchrotron analyses.— TXM analysis utilizes the beam-line #01B1 facility of the National Synchrotron Radiation Research Center (NSRRC) in Taiwan, R.O.C.. The experimental set-up is schematically shown in Fig. 1b. The light source operates with photon energy ranging between 8 and 11 keV. Monochromatic X-rays with specific photon energy are obtained after the white radiations pass through a double crystal monochromator using a pair of Ge (111) crystals. After passing the focusing mirror and Ge DCM, the X-rays are further focused on the electrode inside the coin cell by a capillary condenser

* Electrochemical Society Active Member.
z E-mail: nlw001@ntu.edu.tw; song@nsrrc.org.tw

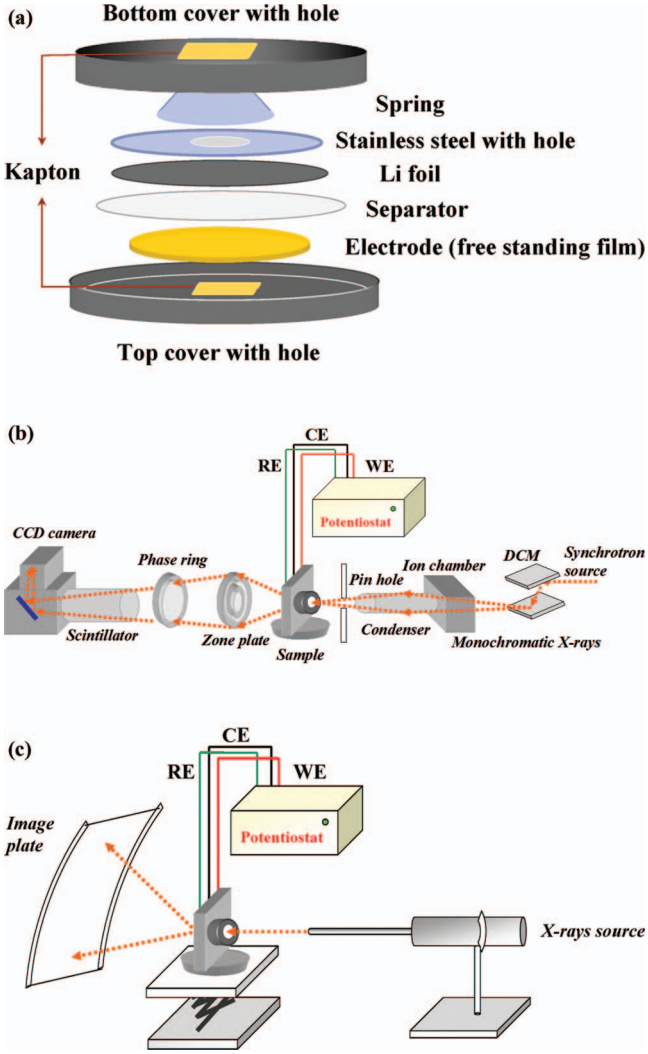

Figure 1. Schematic illustration of (a) the coin-cell assembly for in-situ synchrotron studies; (b) in-situ transmission X-ray microscopy; and (c) in-situ X-ray diffraction. The working electrode in (a) is a free-standing film containing SnO particles embedded within a graphite matrix.

and a pin hole. The transmitted X-rays further go through a zone plate optical system and a phase ring to form the image. The field of view of a single image is 15 × 15 μm for the first order diffraction mode of the zone plate. The phase ring positioned at the back focal plane of the zone plate results in a recording of the phase contrast images at the detector. The electrochemical test was carried out with a potentiostat connected with the coin cell.

Synchrotron X-ray diffraction (XRD) study was conducted by utilizing the facility of the beam-line #01C2 facility (Fig. 1c). The wavelength of the incident X-ray was 1.0223 Å. Each XRD spectrum was obtained with an acquisition time of 240 second. The data was collected using mar345 imaging plate detector. By using FIT2D software, the 2D Debye-Scherrer rings were integrated to the equivalent of 2θ scan and were corrected for polarization and tangent geometry. The scattering angle was calibrated by standard sample, a mixture of silver behenate and silicon powders.

Results and Discussion

Fig. 2 shows the typical morphology of the SnO particles employed in the present study. They are secondary particles composed

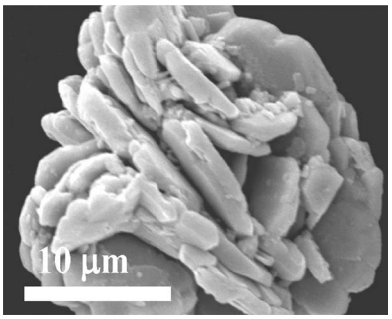

Figure 2. SEM micrograph of the tested SnO partilce.

of strongly sintered plate-like primary particles having a thickness of ca. 2.0 μm.

The voltage-*vs*.-time plot of the SnO(/graphite) electrode under TXM analysis during the first two L/D cycles is shown in Fig. 3a. During this course, a selected SnO particle has been continuously monitored. The dimension of this particle has also been plotted *vs*. time in Fig. 3a. Fig. 3b shows a series of snapshots of this SnO particle. Their corresponding shooting times and voltages are marked by the points shown in Fig. 3a. It is worth noting that a control study has been conducted to expose the electrode to the X-ray beam for 24 hrs without imposing current, and there has been observed no change in the morphology of the SnO particles. Therefore, it can be concluded that the X-ray illumination alone has no effect on the microstructural variations reported in the present study.

TXM micrograph of the fresh particle (panel #1, Fig. 3b) clearly shows the plate characteristics of the primary particles. Upon lithiation, a short plateau first appears at 0.84 V (pt. #2, Fig. 3a) due to the irreversible reduction of SnO to form Sn and Li_2O, as described by reaction 1.[4–6] Below this voltage, the SnO particle is observed to expand over two voltage ranges with momentary stop within ca. 0.5∼0.2 V (i.e., between pts. #3 and #5, Fig. 3a). During the first-stage expansion, between ca. 0.84 ∼ 0.5 V, the dimension increases by ca. 17%, and the plate-shaped interior structure of the particle is more or less retained except that the plates become thicker and they no longer have sharp boundaries (panels #2∼4, Fig. 3b). During the second-stage expansion, below 0.2 V, the particle expands totally to 38%. It becomes increasingly rounded, and the plate-shaped interior structure can no longer be identified (panels #5∼7, Fig. 3b).

In situ XRD analysis (Fig. 4) shows that the intensities of the SnO reflections monotonically decreases, while those of Sn increases, during the first-stage expansion. Lithiated tin compounds, predominantly LiSn and $Li_{22}Sn_5$, appear mainly during the second-stage expansion. (Shifting toward lower Bragg angles of graphite peaks due to Li intercalaction has also been noticed during this stage.) The data indicate that the first-stage expansion is predominantly caused by the reduction of SnO (i.e., reaction 1), while the second-stage is by lithiation of the resulting Sn. The resulting Sn from the first lithiaiton must be in nanometer size, as they can not be individual resolved by TXM and the plate-like morphology of the original particle is mostly retained. No peak due to Li_2O has been detected, indicating that it is in amorphous form.

Upon de-lithiation (panels # 7∼10, Fig. 3b), the particle contracts, and the interior structure of the particle returns back to what was at the beginning of the second-stage (panel #5). Therefore, the second-stage expansion process is completely reversible. The interior structure does not change during the subsequent 3 hr of the rest period (panel #11). During the second (panels #11∼13, Fig. 3b) and third cycles of L/D, the variations in the interior structure of the particle basically follow the second-stage expansion/contraction as observed during the first cycle. The in situ XRD data confirm the reduction of the lithiated compounds with concurrent formation of crystalline Sn upon de-lithiation (Fig. 4).

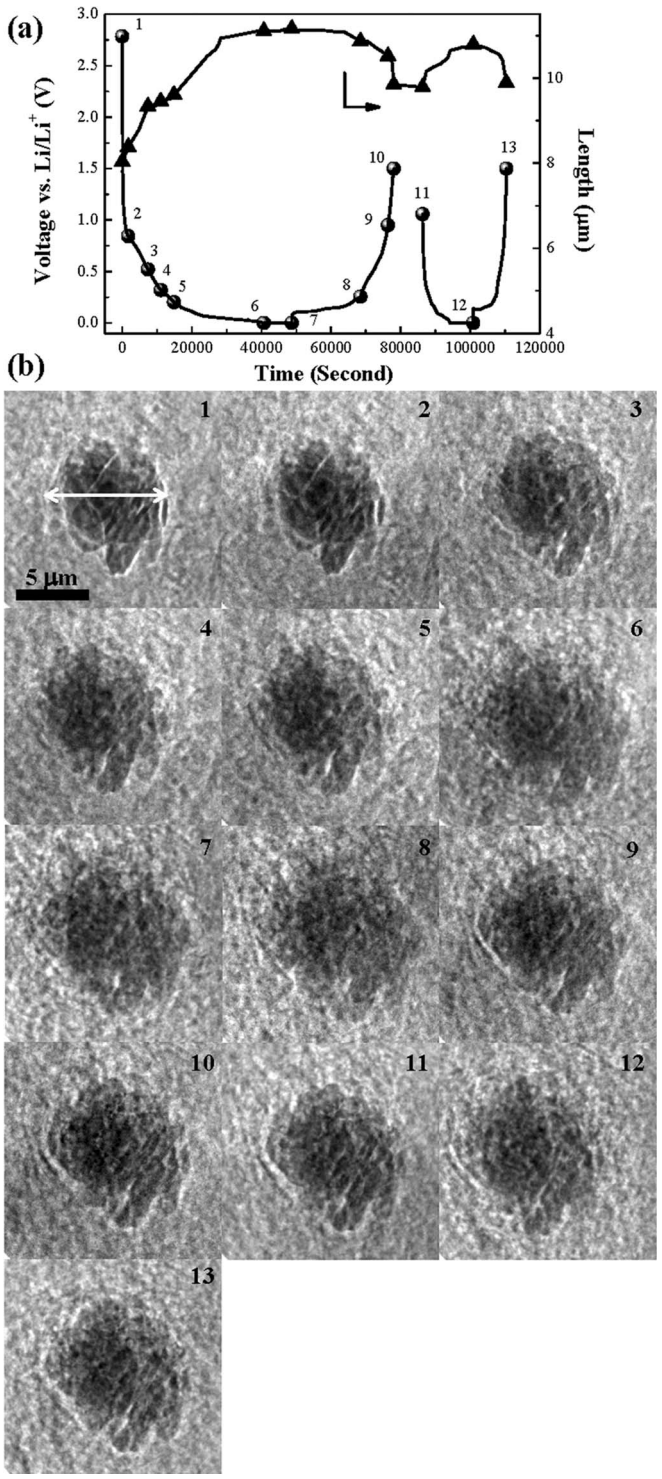

Figure 3. (a) Voltage-vs.-time plot of the SnO electrode and particle dimension-vs.-time plot of the SnO particle shown in (b) during the first two lithiation-delithiation cycles; (b) the snapshots of a selected particle during the same period. The points and numbers shown in (a) mark the moments at which the snapshots of corresponding numbers in (b) have been taken. The arrow in the panel #1 in (b) indicates the direction along which the particle dimensions have been measured.

Based on the data presented above, the following interior structure model, as schematically shown in Fig. 5, is proposed for the SnO particle. Before any L/D, the SnO particle contains plates of primary particles (Fig. 5a). During the first-stage of lithiation, Li_2O is produced, while Sn nano-particles are precipitated within the Li_2O matrix (Fig. 5b). Notably the resulting Li_2O forms the backbone to retain the original particle morphology (plate-like). During the second-stage of lithiation, Sn nano-particles expand due to the formation of Li_xSn phases (Fig. 5c). These nano-particles subsequently de-lithiate and contract back to their original sizes on de-lithiation (Fig. 5d). Throughout the expanding/contracting, the Li_2O backbones are stable to hold together the entire particle so that the particle does not pulverize.

In the previous TXM study on dense Sn particles,[3] we reported the following observations. The expansion process of the Sn particles exhibits strong size dependence with smaller particles expanding faster and earlier (i.e., at higher voltages) than larger particles. A Sn particle of ca. 12 μm, similar to the size of the SnO particle monitored here, has been observed to exhibit sluggish expansion and contraction during the first C/D. Upon the first lithiation, the particle shows first the formation of a very thin lithiated layer and then further lithiation is delayed until the very late stage (the constant-voltage phase) of lithiation where it exhibits burst expansion in rather short period of time. During expansion, the particle shows clear core-shell interior structure until full lithiation. The expanded particle only contract slightly at the end of the de-lithiation, while the interior of the particle continues to change and evolve into porous structure long after de-lithiation.

The SnO particle observed here does not show the core-shell interior structure during expansion. The difference resides in the fact that the SnO particle is a secondary particle consisting of smaller plates and containing open spaces within itself so that all the primary plates can be in direct contact with the electrolyte. As a result, the entire SnO particle undergoes lithiation homogeneously. Lithiation of the dense Sn particle, on the other hand, can only proceed progressively from periphery toward center. Furthermore, the expansion and contraction processes of the SnO during either the first cycle or subsequent cycles take place synchronously with electrochemical L/D without delay (Fig. 3). The prompt deformation response of the active particle to the electrochemical processes may indicate fast lithiation/de-lithiation kinetics. This may be attributed to the fact that the precipitated Sn nano-particles are much smaller than the micron-sized Sn particle, according to the size effect as identified in the previous study.[3]

The strong size-dependence of the expansion/contraction processes as previously observed on the Sn particle can be inferred as follows. Smaller particles have larger surface-to-volume ratios, and hence possess higher overall Li diffuse-in and -out rates per unit mass of the metal. It therefore takes less time for the smaller particles to reach the designated extent of L/D. In addition, considering the potential gradient within the particle, larges particles will require greater polarization at the particle surface in order for complete L/D.

One common phenomenon observed for both anode particles, however, is that the dimensional variations of the particles are not reversible during the first L/D cycle but become so, along with greatly mitigated expansion, during the second and subsequent cycles. Table I summarizes the maximum expansion of the first and second cycles for the two particles. It has been reported[9–17] that the cycling performance

Table I. Maximum expansions of the first two cycles for different Sn-containing particles.

	Cycle number			
	first lithiation		second lithiation	
Material	D_f/D_o (%)[a]	$(D_f/D_o)^3$ (%)	D_f/D_o (%)	$(D_f/D_o)^3$ (%)
Sn[b]	154	365	115	152
SnO	138	262	114	148

[a] D_f and D_o are respectively the linear dimensions of the active particle after and before expansion, as determined from the TXM micrographs along the selected direction indicated in Fig. 2.
[b] from ref. 3.

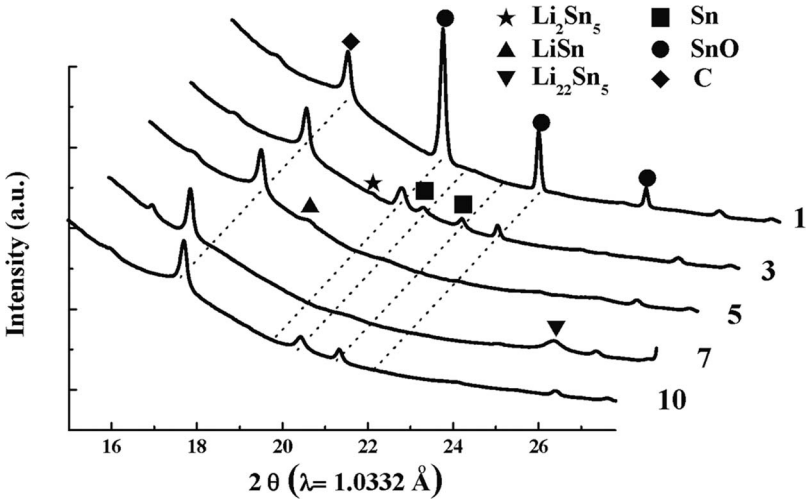

Figure 4. Synchrotron X-ray diffraction data of the SnO electrode acquired during the first lithiation/de-lithiation cycle. The numbers shown to the right end of the curves are same as indicated in Fig. 3.

of lithium alloys can be significantly enhanced if intermetallic or composite hosts are employed instead of pure metal. It has been suggested[9,10,15–17] that the component which is less active or even inactive may serve as a buffering matrix, mitigating the expansion of the active material. The general consensus[4–6] is that the enhanced cycling performance of SnO over Sn is largely due to reduced expansion after the first cycle, owing to the presence of inactive Li_2O. However, as shown in Table I, the expansion ratios of the two particles during the second (and subsequent) cycle are in fact very similar. In contrast, it is the first-cycle expansion ratios of these particles that show large difference. Based on the theoretical densities of all the reactant and product species involved (Sn (7.29 g/cm^3), SnO (6.45), Li_2O (2.01), $Li_{22}Sn_5$ (2.56)), the volume expansion ratios of Sn (356%) and SnO (350%) are almost the same. The observed first-cycle expansion ratio of the previously reported Sn (365%) is very close to the theoretical value (Table I), while the observed ratio of the present SnO, 262%, is much smaller than the theoretical value. The difference is due to the fact that the SnO particle contains much open space within itself (Fig. 2) and that space can accommodate part of the expansion.

It is worth noting that the second cycle is subjected to a much smaller expansion for both particles. Using de-lithiated porous particles as the staring electrode material may get away from the large expansion during the first cycle for both materials, and it may be one way to improve the cycle life of the Li-alloying anodes.

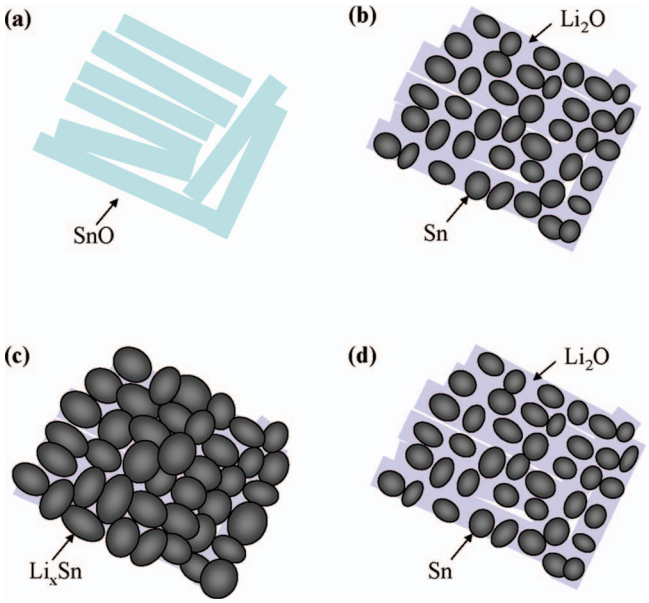

Figure 5. Schematics of the expansion/contraction process of SnO particle during the first cycle of lithiation/de-lithiation: (a) before lithiation; (b) formation of Li_2O and Sn nano-particles after the first stage of expansion; (c) lithiation of Sn nano-particles after the second stage of expansion; and (d) after de-lithiation.

Conclusion

The evolution of the interior microstructures of a SnO particle during electrochemical L/D have been studied by in situ TXM, complemented by in situ XRD to provide phase information. The SnO secondary particle which consists of submicron plates shows homogeneous expansion in two stages during the first lithiation, including the first producing Li_2O backbone that retains most original microstructural features and the second involving lithiation of precipitated Sn nano-particles. These Sn nano-particles readily expand and contract during the subsequent cycles. Overall, the active particle become irreversibly enlarged after the first cycle and exhibit attenuated and reversible expansion/contraction during subsequent cycles. Compared with the dense micron-sized Sn particle previously revealed, the present SnO particle shows much faster L/D kinetics, as indicated by its prompt deformation process, and smaller overall volume expansion. The enhanced kinetics during the second and subsequent cycles is due to the presence of small Sn particles resulting from the first lithiation. The reduced volume expansion is associated with the porous nature of the starting SnO particle. The Li_2O backbones resulting from the first lithiation provides mechanical robustness of the particle, which does not fracture upon cycling.

Acknowledgments

This work is financially supported by National Science Council, National Taiwan University, and Industrial Technology Research Institute in Taiwan. The authors also thank the staff of the Beamline Division of NSRRC for technical support.

References

1. C. J. Wen and R. A. Huggins, *J. Electrochem. Soc.*, **128**, 1181 (1981).
2. R. A. Huggins, *J. Power Sources*, **81–82**, 13 (1999).
3. S. C. Chao, Y. C. Yen, Y. F. Song, Y. M. Chen, H. C. Wu, and N. L. Wu, *Electrochem. Commun.*, **12**, 234 (2010).
4. M. Winter and J. O. Besenhard, *Electrochim. Acta*, **45**, 31 (1999).
5. I. A. Courtney and J. R. Dahn, *J. Electrochem. Soc.*, **144**, 2045 (1997).
6. I. A Courtney, W. R. McKinnon, and J. R. Dahn, *J. Electrochem. Soc.*, **146**, 59 (1999).

7. Y. Idota, T. Kubota, A. Matsufuji, Y. Maekawa, and T. Miyasaka, *Science*, **276**, 1395 (1997).
8. J. Y. Lee, R. Zhang, and Z. Liu, *J. Power Sources*, **90**, 70 (2000).
9. O. Mao, R. L. Turner, I. A. Courtney, B. D. Fredericksen, M. I. Buckett, L. J. Krause, and J. R. Dahn, *Electrochem. Solid-State Lett.*, **2**, 3 (1999).
10. W. R. Liu, N. L. Wu, D. T. Shieh, H. C. Wu, M. H. Yang, C. Korepp, J. O. Besenhard, and M. Winter, *J. Electrochem. Soc.*, **154**, A97 (2007).
11. G. Derrien, J. Hassoun, S. Panero, and B. Scrosati, *Adv. Mater.*, **19**, 2336 (2007).
12. C. M. Park and H. J. Sohn, *Electrochim. Acta*, **54**, 6367 (2009).
13. X. Wang, Z. Wen, B. Lin, J. Lin, X. Wu, and X. Xu, *J. Power Sources*, **184**, 508 (2008).
14. J. T. Vaughey, J. O'Hara, and M. M. Thackeray, *Electrochem. Solid-State Lett.*, **3**, 13 (2000).
15. K. D. Kepler, J. T. Vaughey, and M. M. Thackeray, *J. Power Sources*, **81–82**, 383 (1999).
16. S. Yoon and A. Manthiram, *Chem. Mater.*, **21**, 3898 (2009).
17. S. Matsuno, M. Noji, T. Kashiwagi, M. Nakayama, and M. Wakihara, *J. Phys. Chem. C*, **111**, 7548 (2007).